ACS APPLIED ENERGY MATERIALS

www.acsaem.org Article

A Geometrically Well-Defined and Systematically Tunable Experimental Model to Transition from Planar to Mesoporous Perovskite Solar Cells

Dirk Döhler, Pascal Büttner, Florian Scheler, Dominik Thiel, Bianka Puscher, Sebastian Bochmann, Julian Mitrovic, Pablo P. Boix, Dirk M. Guldi, Ignacio Mínguez-Bacho, and Julien Bachmann*

Cite This: *ACS Appl. Energy Mater.* 2022, 5, 11977−11986 Read Online

ACCESS | Metrics & More | Article Recommendations | Supporting Information

ABSTRACT: A series of perovskite solar cells with systematically varying surface area of the interface between n-type electron conducting layer (TiO_2) and perovskite are prepared by using an ordered array of straight, cylindrical nanopores generated by anodizing an aluminum layer evaporated onto a transparent conducting electrode. A series of samples with pore length varied from 100 to 500 nm are compared to each other and complemented by a classical planar cell and a mesoporous counterpart. All samples are characterized in terms of morphology, chemistry, optical properties, and performance. All samples absorb light to the same degree, and the increased interface area does not generate enhanced recombination. However, the short circuit current density increases monotonically with the specific surface area, indicating improved charge extraction efficiency. The importance of the slow interfacial rearrangement of ions associated with planar perovskite cells is shown to decrease in a systematic manner as the interfacial surface area increases. The results demonstrate that planar and mesoporous cells obey to the same physical principles and differ from each other quantitatively, not qualitatively. Additionally, the study shows that a significantly lower TiO_2 surface area compared to mesoporous TiO_2 is needed for an equal charge extraction.

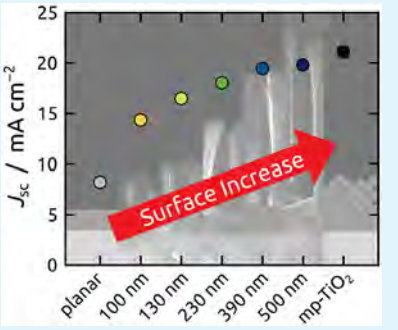

KEYWORDS: *hybrid perovskites, photovoltaics, anodization, ion migration, interface*

INTRODUCTION

Solution-processed hybrid organic−inorganic perovskite solar cells (PSC) have reached an efficiency of 25.6% based on a mesoporous (mp) layer of TiO_2 as the standard electron transport material (ETM) in a n−i−p approach.[1] However, the most recent trend is toward a planar geometry, which offers easier processing, the ability of producing flexible cells, and an easier implementation into tandem cells.[2,3] Unfortunately, switching the geometry from mp to a planar, compact TiO_2 layer leads to a massive drop in efficiency unless specific measures are taken to adjust the TiO_2/perovskite interfaces. Unlike their mp counterparts, planar PSCs based on plain TiO_2 suffer mainly from a low fill factor, a low short circuit current density (J_{sc}), and a severe hysteresis phenomenon—an expression of significant changes in the band alignment over the time scale of many seconds caused by an ion movement.[4−6] To counteract this issue, significant research effort has been invested recently in tuning the electronic structure of planar TiO_2 layers. This has been attempted by doping with ions such as S, Nb, Y, Sm, Mg, Co, Ta/Nb, or Pt[7−14] or by introducing a passivation layer between TiO_2 and the perovskite phase. Several studies have been dedicated to engineered this interface via the addition of ultrathin layers such as inorganic solids, fullerene derivatives, porphyrins, polar solvents, or other kinds of organic molecules to adjust the chemical identity of the surface and thereby fine-tune the band alignment or passivate trap states.[15−22] Both approaches have led to solar cells with over 20% efficiency, yet a stark contrast remains unexplained, namely with mp-TiO_2, with which record efficiencies are achieved without any such TiO_2 and interface engineering.[1,23,24] So far, the planar and mp systems have seemed to be qualitatively different from one another (for unclear reasons), and there has been no attempt to smoothly transition PSCs from the planar case to the mp one, or vice versa.

This transition is precisely the subject of the current paper, in which we demonstrate that in fact, the distinction between planar and mp PSCs is only a quantitative one. The performance parameters can be smoothly transitioned from those of a planar TiO_2-based cell to those of a "classic" mp one by increasing the TiO_2 surface area in a systematic manner (Figure 1).

Received: March 21, 2022
Accepted: August 29, 2022
Published: September 22, 2022

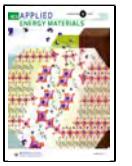

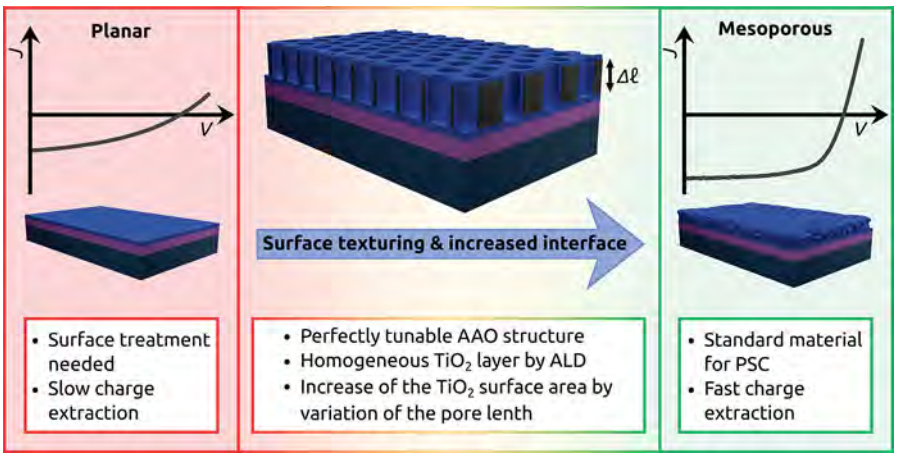

Figure 1. Conceptual sketch of the ordered nanocylindrical nanoporous system as an experimental model that allows one to perform a gradual transition between the "classic" planar and mesoporous types of perovskite solar cells.

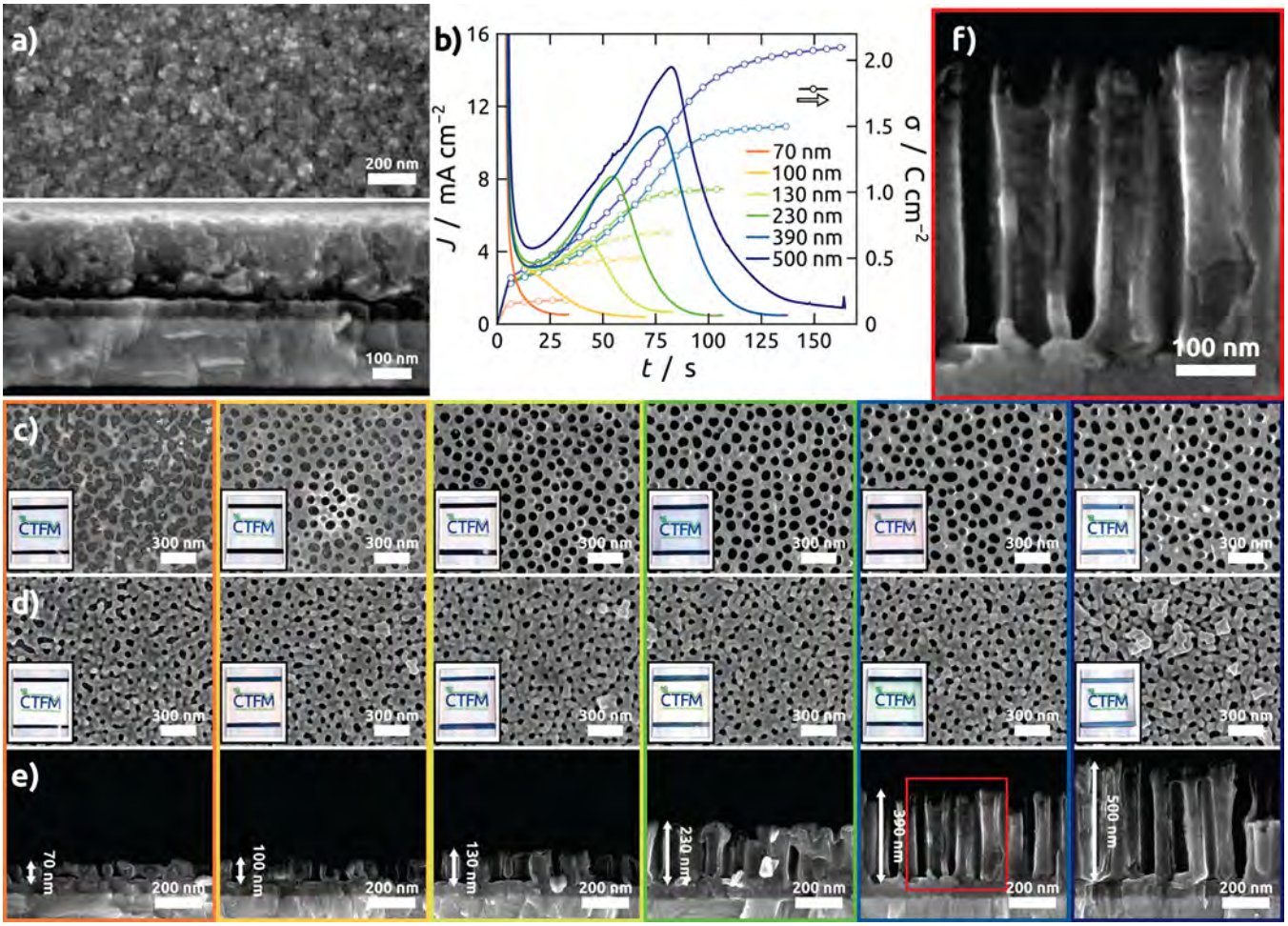

Figure 2. Anodization of Al metal evaporated on a transparent electrode. (a) SEM top view (upper image) and cross section (lower image) of a 200-nm aluminum layer on a glass/ITO/TiO_2 substrate. (b) Anodization current density and surface charge density plotted against anodization time for all AAO pore lengths produced here. (c–e) SEM micrographs of samples with pore lengths of 70, 100, 130, 230, 390, and 500 nm (from left to right) in three situations: (c) in top view after anodization and subsequent pore widening, (d) in top view after further TiO_2 ALD (10 nm) and annealing at 500 °C for 1 h, and (e) in cross section after these steps. The red frame in (e) is enlarged in (f).

To achieve this, we establish an experimentally model system in which the geometry is well-defined and systematically tunable. Anodic aluminum oxide (AAO) is used as a template that provides an ordered array of parallel, straight, cylindrical pores in a chemically inert, electrically insulating matrix.[25−28] These pores are grown by an electrochemical treatment of an aluminum film evaporated on a transparent electrode. This procedure allows one to vary the interpore distance by tuning

https://doi.org/10.1021/acsaem.2c00870
ACS Appl. Energy Mater. 2022, 5, 11977−11986

the voltage and electrolyte, whereas the pore length is defined by the thickness of metallic Al evaporated.[29] Combining these textured substrates with atomic layer deposition (ALD) of TiO_2 enables us to precisely tune the TiO_2 surface area and therefore achieve a stepwise transition from planar to mp-PSC.

After characterization of the materials and performance, we will focus on the incongruity between J_{sc} (from the simple $I-V$ measurement) and the current value obtained by integrating the EQE spectrum. The difference ΔJ_{sc} between these two values provides a reproducible and quantitative measure of the slow changes in band alignment that typically affect planar PSCs with plain TiO_2.[23,30] The physical identity of these changes, most often materialized as a hysteresis in the $I-V$ curve, is still under debate, but it has been attributed to ion motion within the perovskite layer and accumulation at or near the interface to TiO_2.[31−33] Why this effect is so prominent in the planar configuration and not in the mp one has remained unclear. Our results presented below demonstrate that instead of a qualitative difference, there is rather a continuous, quantitative transition from the situation of slow changes (planar) to much faster ones which become experimentally irrelevant (in the mp case).

RESULTS AND DISCUSSION

Preparation. Commercially available glass/ITO slides are used as substrates to deposit the subsequent layer stack. ITO presents a smooth surface that favors homogeneity of the layers deposited on top. We first sputter-coat the ITO substrate with a 50 nm thick compact TiO_2 layer and anneal it at 500 °C to crystallize the layer in the anatase phase. This TiO_2 layer serves a double purpose. First, it acts as an adhesion layer between ITO and Al. Second, it prevents the anodized aluminum oxide (AAO) from lifting off during anodization due to oxygen generation upon consumption of all aluminum.[29,34] Annealing is crucial to improve the conductivity of the sputtered TiO_2 layer and enable homogeneous anodization. The Al layer is then deposited by vacuum evaporation under strict temperature control, necessary to minimize the roughness of the metal film (Figure 2a). (The SEM micrographs of such rough films and subsequent anodization results are shown in Figure S1.) The behavior of the subsequent anodization process can be tracked in current−time curves (Figure 2b), which exhibit three distinct regimes. First, the exponential drop in current density represents the initiation phase of anodization, in which a planar oxide barrier is formed. In the second stage, current increases due to pore formation and growth. Finally, the current drops when all aluminum is consumed. The steady-state regime obtained during anodization of very long pores is never reached here.[29,35] A scanning electron micrograph of pores at this stage is shown in Figure S2. After treatment in 5% phosphoric acid at 45 °C, the pores have an average diameter of 83 nm and a center-to-center distance of 114−126 nm, and the samples are all perfectly transparent (Figure 2c). The regular pore structure is achieved to the same degree for all AAO systems with lengths between 100 and 500 nm, whereas the 70 nm thick layer is less well-defined. When the samples are coated with 16 nm of TiO_2 by ALD, the pore diameter is decreased by 32 nm all along the pore length (Figure 2d−f). The microscopic morphology of all samples from pore length 100 to 500 nm is consistent, whereas slightly different hues are observed on the macroscopic scale (see photographs) resulting from the increased effective refractive index and interference at the air/AAO and AAO/substrate interfaces. Figure 2e allows one to observe the open top extremity of the pores, their parallel order, and the 50 nm thick compact TiO_2 layer underneath. In the magnified micrograph (Figure 2f), the homogeneous TiO_2 coating is apparent.

Table 1 presents all geometric values obtained from microscopic analysis: in addition to the interpore distance d_i, the pore diameter before ALD d_p, and the pore diameter after ALD d_{pa}, we also present the relative surface increase S_{rel} with respect to the planar situation (also called roughness factor). The values obtained between S_{rel} = 1.8 and S_{rel} = 6.7 nicely bridge between the planar situation (defined as S_{rel} = 1) and a mp-TiO_2 layer, evaluated at S_{rel} = 27.3.

Table 1. Summary of Geometric Pore Characteristics Determined before and after Atomic Layer Depositon of TiO_2 by Microscopic Image Analysis[a]

pore length (nm)	d_p (nm)	d_{pa} (nm)	d_i (nm)	S_{rel}
70	85	48	122	1.8
100	81	52	114	2.1
130	82	50	114	2.5
230	82	51	117	3.6
390	85	52	126	5.5
500	82	50	126	6.7

[a]The relative surface increase S_{rel} (also called roughness factor) is defined as the ratio between microscopic surface area and macroscopic (planar) sample area. For cylindrical pore systems, it is calculated from values d_p = 120 nm, d_{pa} = 50 nm, and a surface coverage η_{RCP} = 0.82 for random close packing of hard disks.[36] For the mp case, we consider spheres in random close packing, packing fraction η_{RCP} = 0.64,[36] sphere diameter 17.5 nm, and 120 nm overall thickness.

Materials Characterization. For our system to represent a good model, it is important that only one parameter is varied. Here, we want to vary the surface area without affecting the total light absorption by the perovskite or light scattering by the template. UV−vis transmission spectra measured before and after perovskite infiltration (or, in the planar case, deposition) by spin-coating confirm that this is the case. Figure 3a exhibits well-defined absorption edges for TiO_2 at 380 nm and for the perovskite at 763 nm. Various pore lengths (thicknesses of the AAO matrix) give rise to various interference fringe patterns. In all cases, the transmission of the template is comparable to that of planar or mesoporous samples or even higher. After perovskite deposition, all samples absorb along a highly similar curve from 300 to 763 nm, whereby over the range 550−763 nm the absorption is slightly below quantitative, as often observed for this perovskite stoichiometry.[37,38] The absorption edge corresponds to a bandgap of 1.62−1.63 eV (the corresponding Tauc plots are shown in Figure S3b). In conclusion, any performance differences to be observed between the samples of this series can safely be attributed to electronic effects and are not related light absorption. Photoluminescence (PL) quenching (Figure S4a,b) is observed for all samples compared to perovskite on glass, apart from that no clear trend in the PL quenching is observable. The excitation spectra (Figure S4c) are also all qualitatively similar.

The quality of the perovskite material is demonstrated by X-ray diffraction (XRD) (Figure 3b,c). The intensity of the (101) anatase peak at 25.4° increases with pore length, as expected based on the amount of TiO_2 present. The perovskite is highly crystalline in all cases, with various degrees of orientation. All peaks agree perfectly with literature.[38] The mesoporous system

https://doi.org/10.1021/acsaem.2c00870
ACS Appl. Energy Mater. 2022, 5, 11977−11986

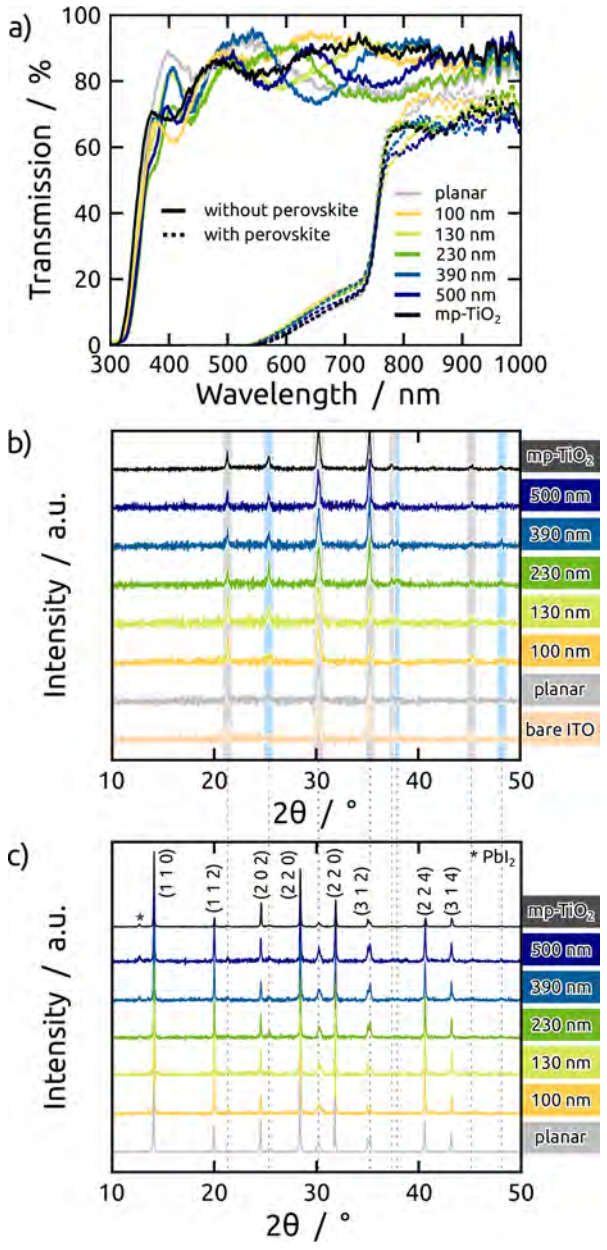

Figure 3. Characterization of samples before and after perovskite infiltration. (a) UV−vis optical transmission spectra. (b) X-ray diffraction (XRD) before infiltration (normalized to the ITO peak at 30.2°); ITO and TiO_2 peaks are highlighted in gray and blue, respectively. (c) XRD after it (normalized to the (110) perovskite peak at 14.1°).

favors the (110) orientation strongly, the planar case is essentially isotropic, and the AAO-templated samples exhibit a moderately enhanced (112) peak at 20.0°. All diffractograms show a peak of similar low intensity at 12.7° indicating the presence of small amounts of lead iodide.

Figure 4a−c documents in microscopic cross-section images the similarity of finished PSCs in planar, mesoporous, and nanoporous geometry, respectively. All cells feature qualitatively the same layer stack, ITO/c-TiO_2 layer/(nanostructured TiO_2 layer)/perovskite/spiro-OMeTAD/gold, and quantitatively total cell thicknesses that are very close to identical (1.0 to 1.1 μm). In detail, the compact, sputtered TiO_2 layer of 45 nm is increased slightly to 61 nm in the AAO-based cells (and the planar one, where 16 nm were also added by ALD for consistency). The hole transporter layer (spiro-OMeTAD) also exhibits minor variations associated with the spin-coated procedure. The total thickness of the perovskite-containing layer is also constant, whereas the compact section of it has a thickness that depends on the presence and nature of the porous layer underneath it. The thickness of the compact perovskite layer for all pore lengths is shown in Figure S5. These observations are in line with the UV−vis transmission data presented above. The perfect infiltration of AAO pores with perovskite is demonstrated directly by a ion-milling preparation of a sample (390 nm long AAO pores) in a plane perpendicular to the pores' long axis (Figure 4d) and by backscattered electron SEM imaging (Figure S6). Both the homogeneous coating of all pores with TiO_2 and their quantitative filling with perovskite are clearly visible.

Functional Performance. After proving that all materials properties, and thereby also the optical functional properties, are comparable whereas the morphology is varied in a systematic manner, we can now turn to the comparison of their solar cell performance. Figure 5a shows the reverse $J-V$ curves (measuring from 1.2 to −0.2 V) of the champion cells of every geometry and every pore length. The planar PSC exhibits the lowest J_{sc} and its curve has an S-shape, whereas the mesoporous cell has the highest J_{sc}, V_{oc}, and fill factor. All nanocylindrical array cells fall in between these two extremes. The evolution of the performance shows a monotonic improvement with the length of the pores from the planar configuration to the mesoporous one (Figure 5b,c,e,f). (Performance data form the forward scans (−0.2 to 1.2 V) are shown in Figure S7.) The overall solar energy conversion efficiency (Figure 5b) increases with interfacial area (quantified here as S_{rel}, often also called the "roughness factor") from about 3% in the planar case to 14% for mesoporous devices. We note that the overall solar energy conversion efficiency of 3% for the planar cell is significantly below the state of the art for this type of cell. Certainly, optimization of the planar devices toward efficiencies close to 20% would be facile as amply demonstrated in the literature.[7−22] However, the goal of this study is to provide the comparison between samples differing only by nanoscale interfacial geometry. Any individual materials optimization of a specific type of samples would render the comparison useless, given that several parameters would have been changed simultaneously. Therefore, let us maintain the materials system and focus on the geometric trends alone:

- The V_{oc} does not contribute to this trend. The constant V_{oc} is a strong indication that the prevalence of carrier recombination in the bulk of the perovskite material does not vary significantly when the cylinder length is varied.
- Furthermore, the behavior of V_{oc} as a function of light intensity (Figure S8a) is similar for all different surface areas, with a linear segment followed by a saturation. This behavior has been described earlier in PSCs,[39] and the ideality factor n_{id} (Figure S8b) can be extracted from the slope in the linear section (Figure S8a). All values are between 1.2 and 1.6, indicative of recombination being prevalent in the immediate vicinity of the interface.[40] This observation further confirms the statement derived above concerning V_{oc} that all devices are dominated by a similar recombination mechanism at or near the interface.
- In part, the fill factor contributes to the $\eta(S_{rel})$ trend (Figure 5c) as it increases almost linearly from 0.35 to about 0.6.

https://doi.org/10.1021/acsaem.2c00870
ACS Appl. Energy Mater. 2022, 5, 11977−11986

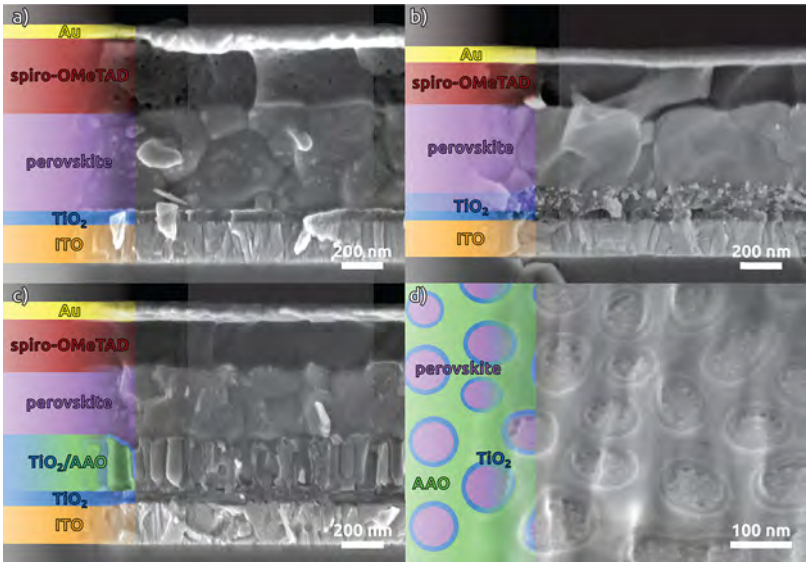

Figure 4. Cross-section of the three different geometries: (a) planar, (b) mesoporous, and (c) AAO pores with the basic device structure of glass/ITO/c-TiO_2/ALD or mp-TiO_2/$Cs_{0.5}(FA_{0.83}MA_{0.17})_{0.95}Pb(I_{0.83}Br_{0.17})_3$/spiro-OMeTAD/Au. (d) Filled AAO pores cut by ion milling of a sample with 390 nm pore length.

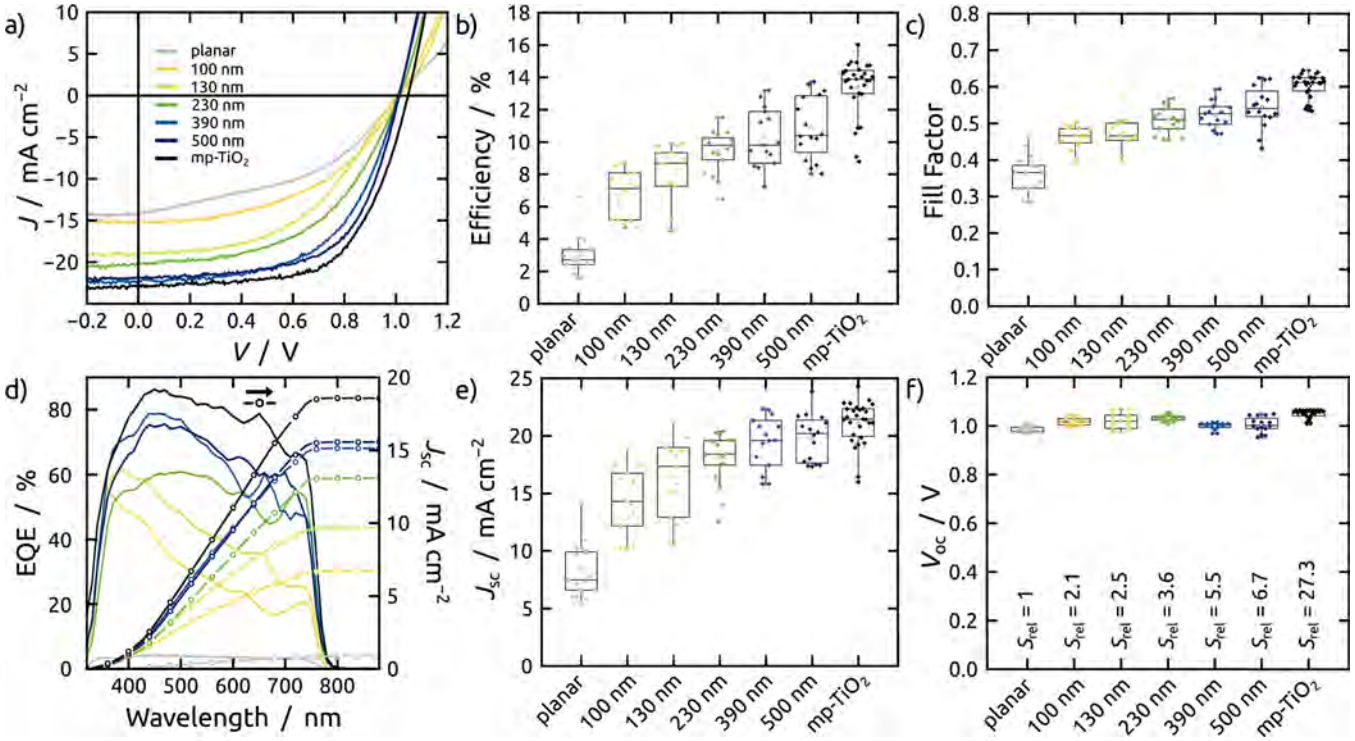

Figure 5. (a) J–V reverse scan (scan speed 50 mV s^{-1}) of the champion cell of each geometry and length. (b) Representative EQE spectra for every geometry and length. Statistical evaluation of efficiency (c), fill factor (d), short circuit current J_{sc} (e), and open circuit potential V_{oc} (f) for all pore lengths and geometries extracted from the reverse scans.

- However, the more important aspect is the evolution of J_{sc} with S_{rel} (Figure 5e). Compared to the planar geometry, the current density is more than doubled for long AAO pores (390–500 nm) and for mesoporous geometry, although the curve flattens out and seems to reach some saturation. Given that the interfacial surface area S_{rel} is varied along this sample series without any changes in light absorption, this increase of current has to be due to a more efficient charge extraction in samples featuring large heterojunction geometric area. We note that when heterostructures of identical morphologies are built without the ALD-TiO_2, the trend is not reproduced (Figure S9). This confirms that the J_{sc} improvement is purely related to charge extraction at the semiconductor junction and not to improved transport properties of the perovskite potentially associated with crystallization in the constrained environment of the porous template.

The same J_{sc} trend is observed when EQE spectra are integrated (Figure 5d). However, the current density values

https://doi.org/10.1021/acsaem.2c00870
ACS Appl. Energy Mater. 2022, 5, 11977–11986

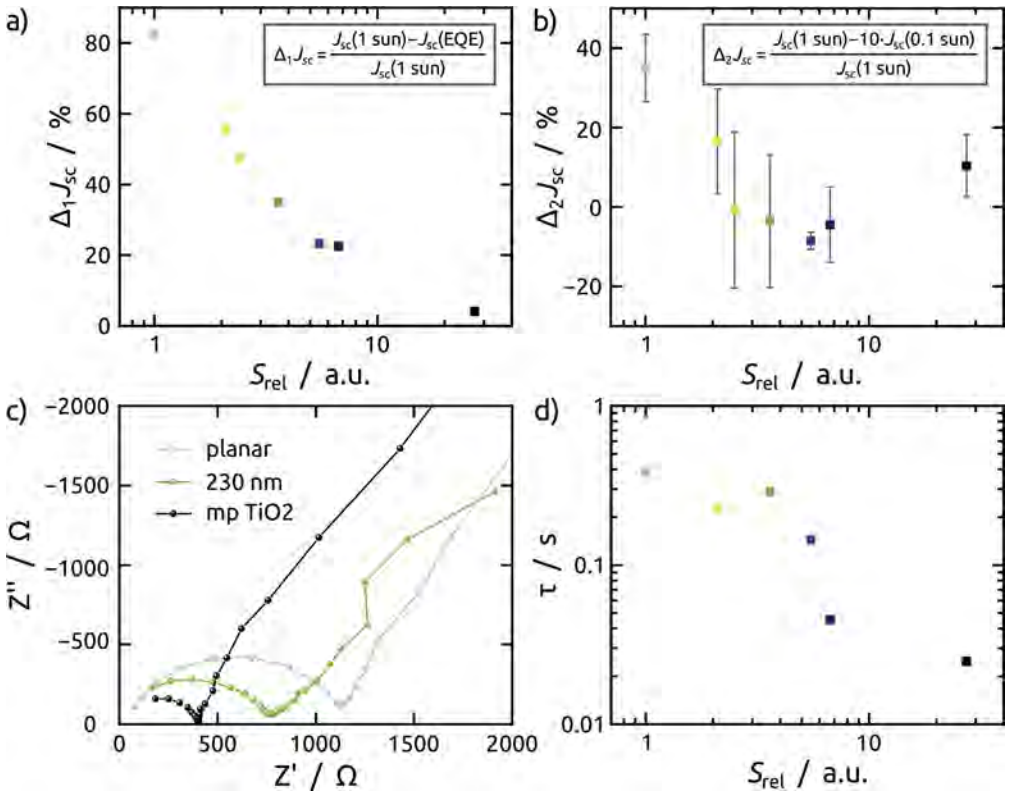

Figure 6. Time scales for ion migration in perovskite cells featuring various specific surface areas S_{rel}. (a) Relative difference $\Delta_1 J_{sc}$ between short circuit current densities determined (1) by integrating the EQE spectrum measured without bias light under 30 Hz chopped single-wavelength irradiation (J_{sc}(EQE)) and (2) under steady-state 1 sun white light irradiation (J_{sc}(1 sun)). (b) A similar analysis using J_{sc} values recorded in high- and low-light conditions confirms that the trend is physically meaningful. (c) Impedance spectroscopy: exemplary set of Nyquist plots recorded at J_{sc} and 0.5 sun on three samples. (d) Evolution of characteristic times extracted from impedance spectroscopy data sets, which follow the same trend and confirm its origin in ionic transport.

obtained from EQE differ significantly from those determined directly from classical $J-V$ measurements, especially for the planar sample and the shorter pores. This incongruity between both values results from slow phenomena occurring under irradiation at or near the interface and is a well-documented fact associated with planar PSCs.[23,41] The shape of the EQE graph is triangular for the short pores, whereas it transitions to a more square shape for longer pores and the mesoporous sample. This hints at extraction issues for charge carriers generated further in the bulk. Given the rather high charge carrier mobilities and diffusion lengths typically similar to the active layer thicknesses used here, the triangular EQE spectrum shape could be related to the formation of a (locally) reversed electric field.[42] EQE measured with a lock-in amplifier and a shutter speed of 30 Hz under very low light intensity is representative of the electronic situation of a sample in the dark, whereas the J_{sc} curve characterizes the quasi-steady-state situation under irradiation and significant current density. In particular, slow ion migration and the charge accumulation at the TiO_2/perovskite interface which are known to occur on the time scale of seconds upon irradiation (and to then revert back to the equilibrium situation in the dark) in planar cells result in significant $\Delta_1 J_{sc} = (J_{sc}(1\text{ sun}) - J_{sc}(EQE))/J_{sc}(1\text{ sun})$. This difference is in contrast to planar cells, virtually absent from cells built on mp TiO_2/perovskite interface. This trend in the difference $\Delta_1 J_{sc}$ between measured and integrated current densities becomes obvious in Figure 6a. That this trend is physically meaningful can be confirmed with another way of comparing high- and low-light conditions: $\Delta_2 J_{sc} = (J_{sc}(1\text{ sun}) - 10 J_{sc}(0.1\text{ sun}))/J_{sc}(1\text{ sun})$ yields a similar trend (Figure 6b). It demonstrates a gradual transition between planar and mp situations, in contrast to the dichotomy suggested by the literature.[43] In other words, ion accumulation (or depletion) at interfaces, which "turn on" charge injection in what has been described as an ionically gated transistor interface,[32,33] is not a phenomenon specific to planar PSCs but one that is common to PSCs of all geometries. Its influence decreases gradually when the interface surface area increases. What could be the mechanism for this gradual change? If a certain density of mobile ions is needed to accumulate charges and gate the interface, then the large specific surface area shortens the maximum distances that ions must move to reach the interface. Drawing ions from a given volume of perovskite is rendered possible at shorter distances from the interface if the interface is nanostructured to a large specific surface area.

Further confirmation for the origin of this trend can be gained by impedance spectroscopy—a frequency-dependent technique that can identify processes with different time responses within the device. We analyzed the impedance spectra for devices under 0.5 sun intensity at short circuit. The resulting Nyquist plots reproduce the two distinctive arcs of perovskite solar cells,[44] as displayed for representative devices in Figure 6c. The smaller arc, corresponding to the high-frequency region, shrinks as the device surface area increases. This could be classically attributed to a recombination enhancement. However, the quasi-invariant V_{oc} values do not support this interpretation. Besides, while impedance spectroscopy for solar cells is usually measured at voltages higher than short circuit conditions to understand recombination processes, here we focus on short-circuit

https://doi.org/10.1021/acsaem.2c00870
ACS Appl. Energy Mater. 2022, 5, 11977−11986

conditions, where the recombination resistance is usually much larger and not necessarily dominating the cell response. The results are fitted to a simplified equivalent circuit (presented in Figure S11) developed elsewhere,[45] which includes a resistor usually attributed to transport and recombination processes (R_{tr+rec}) in parallel with the geometric capacitance of the device (C_{geo}) and a low-frequency branch with a capacitor (C_{dr}) and resistor (R_{dr}), both related to the ionic nature of the perovskites, in parallel to the rest of the branches. To account for dispersive relaxation processes, the capacitors are modeled by constant phase elements. The combination of the dominant capacitance (C_{dr}) and resistance (R_{tr+rec}) can be used to calculate a characteristic time $\tau = R_{tr+rec}C_{dr}$. This value falls in the range of 1−0.01 s expected for ionic motion.[46,47] Interestingly, the distinctive times, presented in Figure 6d, decrease significantly as the surface area increases, in a manner that reproduces the trends in Figure 6a,b. The slower response in the devices with smaller effective surfaces confirms the ΔJ_{sc} as originating from ionic motion, which is emphasized under lower charge concentration conditions (low light intensities), where the ionic conductivity dominates.

CONCLUSIONS

Much has been said about hysteresis in the $J-V$ curves of perovskite solar cells, about slow physical changes in the vicinity of the perovskite/TiO_2 interface, and about the chemical nature of those changes. The literature is rife with contradictions and apparent contradictions related to the fact that no two PSCs are identical with one another. A consensus has emerged over the past few years, according to which planar TiO_2 PSCs are particularly affected by these slow rearrangements (associated with ion migration to the interface, whereby ion accumulation gates charge transfer across it), unless the interface is subjected to a preliminary treatment that circumvents the need for them. Mesoporous PSCs have seemed to be largely unaffected by these rearrangements. This contrast between what seem to be two qualitatively different behaviors of two materials systems that differ only in their geometry contradicts a logic based on the identical chemical identity of TiO_2-based planar and mp-PSCs.

The model system presented here offers the chance to articulate a continuity of behaviors between these two extremes. Having an ordered system of straight, cylindrical pores as a matrix allows the experimentalist to vary the specific surface area of the TiO_2/perovskite interface in a systematic manner and to observe directly how each performance parameter is affected by it. What we discover is that far from being completely distinct from each other, mp-PSCs and planar PSCs are simply two extremes of the same family. While planar PSCs need time to draw ions from a certain volume of perovskite, their counterparts presenting a nanostructured, high-surface-area interface can draw them from a similar volume situated at shorter distances from the interface. Thus, ion migration reaches the steady state much faster, on a time scale that is no longer relevant in most measurements.

We are convinced that the nanoporous 'anodic' PSCs presented will be used to address other aspects of PSCs or further similar devices, and can contribute to clarifying and organizing various aspects of PSC knowledge that have remained confusing in the recent literature.

EXPERIMENTAL SECTION

Sample Preparation. ITO-coated glass substrates purchased from Techinstro with a sheet resistance of 10 Ω/□ are first cleaned by sonication in Hellmanex III (2% in Millipore water), acetone, and isopropanol for 5 min each and subjected to UV-ozone cleaning (Novascan PSD-UV4) for 30 min before use. A blocking layer of 45 nm amorphous TiO_2 (TiO_2 target, 99.99%) is deposited by radio-frequency sputtering (CRC 622 model, Torr International, Inc.) at a working pressure of 4.3 Pa with a power density of 2.5 W cm^{-2}, resulting in a deposition rate of 0.1 Å s^{-1}. Afterward, the samples are annealed at 500 °C for 1 h on a hot plate in air. Immediately before Al deposition the substrates are again cleaned by a UV-ozone treatment for 30 min. 60, 90, 110, 200, 340, and 440 nm of Al film are thermally evaporated from Al pellets (99.999%, Ångstrom Engeneering Inc.) with a Covap system from Ångstrom Engenieering Inc. The deposition rate is 1.3 Å s^{-1}. 340 and 440 nm are deposited in two steps separated by a cool-down pause.

The Al thin films are anodized at 0 °C with a Keithley SourceMeter 2450 in a two-electrode setup in an 0.3 M oxalic acid electrolyte at 60 V. The end point of anodization is indicated by the anodization current reaching a minimum and the sample turning transparent. Thereafter, the pores are widened in 5 wt % H_3PO_4 at 45 °C for 10 min, directly rinsed with deionized water, and finally dried with N_2.

TiO_2 ALD is performed with an Arradiance Gemstar XT benchtop reactor. Precursor pulse times for titanium(IV) isopropoxide (TTIP, Alfa Aesar) and water, exposure times, and purge times are 1, 0.5, 25, and 60 s, respectively. TTIP and water are kept at 70 °C and room temperature, respectively. The chamber temperature is 150 °C. The deposition rate is 0.5 Å $cycle^{-1}$, and 16 nm is deposited. Subsequently, the samples are annealed at 500 °C for 1 h on a hot plate in ambient air.

For the mp-TiO_2 samples, 150 mg mL^{-1} titanium nanoxide T/SP (Solaronix) in ethanol is spin-coated at 4000 rpm with an acceleration of 2000 rpm s^{-1} for 10 s. Thereafter, they are dried for 10 min at 100 °C and annealed at 500 °C for 1 h in ambient air. After cooling, they are UV-ozone cleaned for 30 min and directly transferred to a N_2-filled glovebox for perovskite deposition.

The perovskite solution is processed as suggested by Saliba et al.[24] 0.2 g of formamidinium iodide (FAI) and 0.05 g of methylammonium bromide (MABr) are dissolved in 0.936 mL of PbI_2 solution (1.5 M, 4:1 DMF:DMSO) or 0.352 mL of $PbBr_2$ solution (1.5 M, 4:1 DMF:DMSO), respectively. (All chemicals were purchased from Sigma-Aldrich.) For the final perovskite solution these solutions are mixed in a 5:1 ratio $FAPbI_3$:$MAPbBr_3$, and 5% CsI stock solution (1.5 M in DMSO) is added. This solution is directly spin-coated on the samples in a two-step process: 1000 rpm (acceleration 500 rpm s^{-1}) for 10 s, ramp with 1000 rpm s^{-1} to 6000 rpm for 20 s. Finally, 800 μL of chlorobenzene (Merck) is added 10 s before the end.

The $N^2,N^2,N^{2\prime},N^{2\prime},N^7,N^7,N^{7\prime},N^{7\prime}$-octakis(4-methoxyphenyl)-9,9′-spirobi[9*H*-fluorene]2,2′,7,7′-tetramine (spiro-OMeTAD) solution is prepared in a N_2-filled glovebox as suggested by Saliba et al.[37] To a 70 mM solution of spiro-OMeTAD in chlorobenzene bis(trifluoromethane)sulfonimide lithium salt (Li-TFSI) (520 mg mL^{-1} in acetonitrile), tris(2-(1*H*-pyrazol-1-yl)-4-*tert*-butylpyridine)cobalt(III) tri[bis(trifluoromethane)sulfonimide] (FK209) (200 mg mL^{-1} in acetonitrile), and 4-*tert*-butylpyridine are added in a molar ratio of 0.5/0.03/3.3 with respect to spiro-OMeTAD. (All chemicals were purchased from Sigma-Aldrich.) The solution is then filtered with a 0.45 μm PTFE filter and spin-coated with 4000 rpm for 20 s with an acceleration of 2000 rpm s^{-1}. Subsequently, the samples are taken out of the glovebox and left in air overnight. 80 nm Au is evaporated with an Covap evaporator from Ångstrom Engineering with a deposition rate of 1.2 Å s^{-1} (0.5 Å s^{-1} first 10 nm). The active area is 0.075 cm^2.

Characterization. The thickness of the as-grown ALD layers and the sputtered layers is measured by spectroscopic ellipsometry (SENpro, Sentech). For SEM micrographs, a JEOL JMS-F100 or Zeiss Gemini 500s field-emission instrument is used. Pore diameters are measured with the open source software ImageJ, and the interpore distance is measured by using self-correlation images obtained with the software WSxM (ver. 5.0 Develop 8.3).[48,49] Ion milling preparation is done with a Jeol IB-19530CP cross-section polisher. XRD diffractograms are recorded on a Bruker D8 Advance with a Cu Kα source and a LynxEye XE-T detector. Optical transmission spectra are measured with a DH-2000-L light source and a HR4000 spectrometer form

https://doi.org/10.1021/acsaem.2c00870
ACS Appl. Energy Mater. 2022, 5, 11977−11986

Ocean Optics. Steady-state fluorescence spectra are measured with a Edinburgh Instruments FS-5 fluorometer (slits: 5 nm; integration time: 0.2 s). For the emission spectra a excitation wavelength of 532 nm is used. A solar simulator (Newport) equipped with a Xe lamp source is calibrated to AM1.5 (100 mW cm^{-2}) with a reference Si solar cell (Newport) used a light source. Photovoltaic characterization is performed in ambient conditions. Electrical data are recorded by using a single-channel Gamry Reference 600 potentiostat. The scan rate is set to 50 mV s^{-1}, and the scan range is from −0.2 to 1.2 V and reverse. EQE spectra are measured by using a QEPVSI-b setup by Oriel equipped with a 300 W Xe light source, a monochromator, and a lock-in amplifier. The shutter frequency is set to 30 Hz.

■ ASSOCIATED CONTENT

Supporting Information

The Supporting Information is available free of charge at https://pubs.acs.org/doi/10.1021/acsaem.2c00870.

Figure S1: scanning electron micrographs of an aluminum layer with insufficient thermal control during deposition and of pores obtained from it; Figure S2: scanning electron micrograph of an AAO template directly after anodization at 60 V without pore widening; Figure S3: Tauc plots of the TiO_2 and the perovskite absorption edges; Figure S4: steady-state fluorescence measurements; Figure S5: thickness of the compact perovskite layer on top of the AAO structure plotted against the pore length; Figure S6: backscattered electron SEM cross-section micrograph showing perfect pore filling; Figure S7: performance parameters for the $J-V$ forward curves measured from 0.2 to 1.2 V; Figure S8: open circuit potentials plotted against light intensity and ideality factors; Figure S9: performance parameters of the $J-V$ curves of AAO PSCs without TiO_2 ALD; Figure S10: $J-V$ curves recorded at various scan rates for various samples; Figure S11: equivalent circuit model used to fit the impedance data (PDF)

■ AUTHOR INFORMATION

Corresponding Author

Julien Bachmann − *Chemistry of Thin Film Materials, Department of Chemistry and Pharmacy, Friedrich-Alexander-Universität Erlangen-Nürnberg, 91058 Erlangen, Germany;* orcid.org/0000-0001-6480-6212; Email: julien.bachmann@fau.de

Authors

Dirk Döhler − *Chemistry of Thin Film Materials, Department of Chemistry and Pharmacy, Friedrich-Alexander-Universität Erlangen-Nürnberg, 91058 Erlangen, Germany*

Pascal Büttner − *Chemistry of Thin Film Materials, Department of Chemistry and Pharmacy, Friedrich-Alexander-Universität Erlangen-Nürnberg, 91058 Erlangen, Germany*

Florian Scheler − *Chemistry of Thin Film Materials, Department of Chemistry and Pharmacy, Friedrich-Alexander-Universität Erlangen-Nürnberg, 91058 Erlangen, Germany*

Dominik Thiel − *Interdisciplinary Center for Molecular Materials (ICMM), Department of Chemistry and Pharmacy, Friedrich-Alexander-Universität Erlangen-Nürnberg, 91058 Erlangen, Germany*

Bianka Puscher − *Interdisciplinary Center for Molecular Materials (ICMM), Department of Chemistry and Pharmacy, Friedrich-Alexander-Universität Erlangen-Nürnberg, 91058 Erlangen, Germany*

Sebastian Bochmann − *Chemistry of Thin Film Materials, Department of Chemistry and Pharmacy, Friedrich-Alexander-Universität Erlangen-Nürnberg, 91058 Erlangen, Germany*

Julian Mitrovic − *Chemistry of Thin Film Materials, Department of Chemistry and Pharmacy, Friedrich-Alexander-Universität Erlangen-Nürnberg, 91058 Erlangen, Germany*

Pablo P. Boix − *Instituto de Ciencia de Materiales, Universidad de Valencia, 46980 Paterna, Spain;* orcid.org/0000-0001-9518-7549

Dirk M. Guldi − *Interdisciplinary Center for Molecular Materials (ICMM), Department of Chemistry and Pharmacy, Friedrich-Alexander-Universität Erlangen-Nürnberg, 91058 Erlangen, Germany;* orcid.org/0000-0002-3960-1765

Ignacio Mínguez-Bacho − *Chemistry of Thin Film Materials, Department of Chemistry and Pharmacy, Friedrich-Alexander-Universität Erlangen-Nürnberg, 91058 Erlangen, Germany;* orcid.org/0000-0003-1680-1729

Complete contact information is available at: https://pubs.acs.org/10.1021/acsaem.2c00870

Notes

The authors declare no competing financial interest.

■ ACKNOWLEDGMENTS

We thank Sofia Korenko for preparing some substrates. We thank Nicolas Vogel for the opportunity to use his Gemini 500s electron microscope. This work was funded by the European Research Council with a Consolidator Grant ("Solacylin", grant agreement 647281). P.P.B. acknowledges the funding by MCIN/AEI and FEDER (project with reference MAT2017-88905-P) and a Ramon y Cajal grant.

■ REFERENCES

(1) Jeong, J.; Kim, M.; Seo, J.; Lu, H.; Ahlawat, P.; Mishra, A.; Yang, Y.; Hope, M. A.; Eickemeyer, F. T.; Kim, M.; Yoon, Y. J.; Choi, I. W.; Darwich, B. P.; Choi, S. J.; Jo, Y.; Lee, J. H.; Walker, B.; Zakeeruddin, S. M.; Emsley, L.; Rothlisberger, U.; Hagfeldt, A.; Kim, D. S.; Grätzel, M.; Kim, J. Y. Pseudo-Halide Anion Engineering for α-$FAPbI_3$ Perovskite Solar Cells. *Nature* **2021**, *592*, 381−385.

(2) Zhang, W.; Wang, Y.-C.; Li, X.; Song, C.; Wan, L.; Usman, K.; Fang, J. Recent Advance in Solution-Processed Organic Interlayers for High-Performance Planar Perovskite Solar Cells. *Adv. Sci.* **2018**, *5*, 1800159.

(3) Jošt, M.; Kegelmann, L.; Korte, L.; Albrecht, S. Monolithic Perovskite Tandem Solar Cells: A Review of the Present Status and Advanced Characterization Methods Toward 30% Efficiency. *Adv. Energy Mater.* **2020**, *10*, 1904102.

(4) Alberti, A.; Smecca, E.; Sanzaro, S.; Bongiorno, C.; Giannazzo, F.; Mannino, G.; La Magna, A.; Liu, M.; Vivo, P.; Listorti, A.; Calabrò, E.; Matteocci, F.; Di Carlo, A. Nanostructured TiO_2 Grown by Low-Temperature Reactive Sputtering for Planar Perovskite Solar Cells. *ACS Appl. Energy Mater.* **2019**, *2*, 6218−6229.

(5) Li, H.; Li, C.; Wen, S.; Wang, C.; Wang, G.; Li, C.; Wang, C.; Huang, L.; Dong, W.; Ruan, S. Suppressing TiO_2/Perovskite Interfacial Electron Trapping in Perovskite Solar Cell for Efficient Charge Extraction and Improved Device Performance. *ACS Sust. Chem. Eng.* **2018**, *6*, 11295−11302.

(6) Liu, P.; Wang, W.; Liu, S.; Yang, H.; Shao, Z. Fundamental Understanding of Photocurrent Hysteresis in Perovskite Solar Cells. *Adv. Energy Mater.* **2019**, *9*, 1803017.

(7) Sun, H.; Xie, D.; Song, Z.; Liang, C.; Xu, L.; Qu, X.; Yao, Y.; Li, D.; Zhai, H.; Zheng, K.; Cui, C.; Zhao, Y. Interface Defects Passivation and Conductivity Improvement in Planar Perovskite Solar Cells Using Na_2S-Doped Compact TiO_2 Electron Transport Layers. *ACS Appl. Mater. Interfaces* **2020**, *12*, 22853−22861.
(8) Xiao, G.; Shi, C.; Lv, K.; Ying, C.; Wang, Y. Nb-Doping TiO_2 Electron Transporting Layer for Efficient Perovskite Solar Cells. *ACS Appl. Energy Mater.* **2018**, *1*, 2576−2581.
(9) Zhou, H.; Chen, Q.; Li, G.; Luo, S.; Song, T.-b.; Duan, H.-S.; Hong, Z.; You, J.; Liu, Y.; Yang, Y. Interface Engineering of Highly Efficient Perovskite Solar Cells. *Science* **2014**, *345*, 542.
(10) Xiang, Y.; Ma, Z.; Zhuang, J.; Lu, H.; Jia, C.; Luo, J.; Li, H.; Cheng, X. Enhanced Performance for Planar Perovskite Solar Cells with Samarium-Doped TiO_2 Compact Electron Transport Layers. *J. Phys. Chem. C* **2017**, *121*, 20150−20157.
(11) Wang, J.; Qin, M.; Tao, H.; Ke, W.; Chen, Z.; Wan, J.; Qin, P.; Xiong, L.; Lei, H.; Yu, H.; Fang, G. Performance Enhancement of Perovskite Solar Cells With Mg-Doped TiO_2 Compact Film As the Hole-Blocking Layer. *Appl. Phys. Lett.* **2015**, *106*, 121104.
(12) Ren, X.; Xie, L.; Kim, W. B.; Lee, D. G.; Jung, H. S.; Liu, S. F. Chemical Bath Deposition of Co-Doped TiO_2 Electron Transport Layer for Hysteresis-Suppressed High-Efficiency Planar Perovskite Solar Cells. *Sol. RRL* **2019**, *3*, 1900176.
(13) Duan, Y.; Zhao, G.; Liu, X.; Ma, J.; Chen, S.; Song, Y.; Pi, X.; Yu, X.; Yang, D.; Zhang, Y.; Guo, F. Low-Temperature Processed Tantalum/Niobium Co-Doped TiO_2 Electron Transport Layer for High-Performance Planar Perovskite Solar Cells. *Nanotechnol.* **2021**, *32*, 245201.
(14) Jiang, L.-L.; Wang, Z.-K.; Li, M.; Li, C.-H.; Fang, P.-F.; Liao, L.-S. Enhanced Electrical Property of Compact TiO_2 Layer via Platinum Doping for High-Performance Perovskite Solar Cells. *Sol. RRL* **2018**, *2*, 1800149.
(15) Li, W.; Zhang, W.; Van Reenen, S.; Sutton, R. J.; Fan, J.; Haghighirad, A. A.; Johnston, M. B.; Wang, L.; Snaith, H. J. Enhanced UV-Light Stability of Planar Heterojunction Perovskite Solar Cells With Caesium Bromide Interface Modification. *Energy Environ. Sci.* **2016**, *9*, 490−498.
(16) Ma, J.; Chang, J.; Lin, Z.; Guo, X.; Zhou, L.; Liu, Z.; Xi, H.; Chen, D.; Zhang, C.; Hao, Y. Elucidating the Roles of $TiCl_2$ and PCBM Fullerene Treatment on TiO_2 Electron Transporting Layer for Highly Efficient Planar Perovskite Solar Cells. *J. Phys. Chem. C* **2018**, *122*, 1044−1053.
(17) Wang, B.; Yang, J.; Lu, L.; Xiao, W.; Wu, H.; Xiong, S.; Tang, J.; Duan, C.; Bao, Q. Interface Engineering of Air-Stable n-Doping Fullerene-Modified TiO_2 Electron Transport Layer for Highly Efficient and Stable Perovskite Solar Cells. *Adv. Mater. Interfaces* **2020**, *7*, 1901964.
(18) Gkini, K.; Balis, N.; Papadakis, M.; Verykios, A.; Skoulikidou, M.-C.; Drivas, C.; Kennou, S.; Golomb, M.; Walsh, A.; Coutsolelos, A. G.; Vasilopoulou, M.; Falaras, P. Manganese Porphyrin Interface Engineering in Perovskite Solar Cells. *ACS Appl. Energy Mater.* **2020**, *3*, 7353−7363.
(19) Yu, J. C.; Kim, D. B.; Baek, G.; Lee, B. R.; Jung, E. D.; Lee, S.; Chu, J. H.; Lee, D.-K.; Choi, K. J.; Cho, S.; Song, M. H. High-Performance Planar Perovskite Optoelectronic Devices: A Morphological and Interfacial Control by Polar Solvent Treatment. *Adv. Mater.* **2015**, *27*, 3492−3500.
(20) Jiang, J.; Jin, Z.; Lei, J.; Wang, Q.; Zhang, X.; Zhang, J.; Gao, F.; Liu, S. F. ITIC Surface Modification to Achieve Synergistic Electron Transport Layer Enhancement for Planar-Type Perovskite Solar Cells With Efficiency Exceeding 20%. *J. Mater. Chem. A* **2017**, *5*, 9514−9522.
(21) Qiu, L.; Ono, L. K.; Jiang, Y.; Leyden, M. R.; Raga, S. R.; Wang, S.; Qi, Y. Engineering Interface Structure to Improve Efficiency and Stability of Organometal Halide Perovskite Solar Cells. *J. Phys. Chem. B* **2018**, *122*, 511−520.
(22) Pérez-del Rey, D.; Boix, P. P.; Sessolo, M.; Hadipour, A.; Bolink, H. J. Interfacial Modification for High-Efficiency Vapor-Phase-Deposited Perovskite Solar Cells Based on a Metal Oxide Buffer Layer. *J. Phys. Chem. Lett.* **2018**, *9*, 1041−1046.
(23) Chen, W.; Yin, X.; Que, M.; Xie, H.; Liu, J.; Yang, C.; Guo, Y.; Wu, Y.; Que, W. A Comparative Study of Planar and Mesoporous Perovskite Solar Cells With Printable Carbon Electrodes. *J. Power Sources* **2019**, *412*, 118−124.
(24) Saliba, M.; Correa-Baena, J.-P.; Wolff, C. M.; Stolterfoht, M.; Phung, N.; Albrecht, S.; Neher, D.; Abate, A. How to Make over 20% Efficient Perovskite Solar Cells in Regular (n-i-p) and Inverted (p-i-n) Architectures. *Chem. Mater.* **2018**, *30*, 4193−4201.
(25) Nielsch, K.; Choi, J.; Schwirn, K.; Wehrspohn, R. B.; Gösele, U. Self-ordering Regimes of Porous Alumina: The 10% Porosity Rule. *Nano Lett.* **2002**, *2*, 677−680.
(26) Mínguez-Bacho, I.; Scheler, F.; Büttner, P.; Bley, K.; Vogel, N.; Bachmann, J. Ordered Nanopore Arrays With Large Interpore Distances via One-Step Anodization. *Nanoscale* **2018**, *10*, 8385−8390.
(27) de Melo, O.; Larramendi, E. M.; Bacho, I. M.; Larramendi, S.; Baldonedo, J. L.; Duart, J. M. M.; Hernández-Vélez, M. Growth of CdSe and CdTe Crystals Shaped by Thick Alumina Membranes. *J. Cryst. Growth* **2008**, *311*, 26−31.
(28) Prida, V. M.; Vega, V.; García, J.; Iglesias, L.; Hernando, B.; Minguez-Bacho, I.; Vázquez, M. *Magnetic Nano- and Microwires*; Woodhead Publishing: 2015; pp 3−39.
(29) Döhler, D.; Triana, A.; Büttner, P.; Scheler, F.; Goerlitzer, E. S. A.; Harrer, J.; Vasileva, A.; Metwalli, E.; Gruber, W.; Unruh, T.; Manshina, A.; Vogel, N.; Bachmann, J.; Mínguez-Bacho, I. A Self-Ordered Nanostructured Transparent Electrode of High Structural Quality and Corresponding Functional Performance. *Small* **2021**, *17*, 2100487.
(30) Vaenas, N.; Konios, D.; Stergiopoulos, T.; Kymakis, E. Slow Photocharging and Reduced Hysteresis in Low-Temperature Processed Planar Perovskite Solar Cells. *RSC Adv.* **2015**, *5*, 107771−107776.
(31) Weber, S. A. L.; Hermes, I. M.; Turren-Cruz, S.-H.; Gort, C.; Bergmann, V. W.; Gilson, L.; Hagfeldt, A.; Graetzel, M.; Tress, W.; Berger, R. How the Formation of Interfacial Charge Causes Hysteresis in Perovskite Solar Cells. *Energy Environ. Sci.* **2018**, *11*, 2404−2413.
(32) Jacobs, D. A.; Shen, H.; Pfeffer, F.; Peng, J.; White, T. P.; Beck, F. J.; Catchpole, K. R. The Two Faces of Capacitance: New Interpretations for Electrical Impedance Measurements of Perovskite Solar Cells and Their Relation to Hysteresis. *J. Appl. Phys.* **2018**, *124*, 225702.
(33) Moia, D.; Gelmetti, I.; Calado, P.; Fisher, W.; Stringer, M.; Game, O.; Hu, Y.; Docampo, P.; Lidzey, D.; Palomares, E.; Nelson, J.; Barnes, P. R. F. Ionic-to-Electronic Current Amplification in Hybrid Perovskite Solar Cells: Ionically Gated Transistor-Interface Circuit Model Explains Hysteresis and Impedance of Mixed Conducting Devices. *Energy Environ. Sci.* **2019**, *12*, 1296−1308.
(34) Foong, T. R. B.; Sellinger, A.; Hu, X. Origin of the Bottlenecks in Preparing Anodized Aluminum Oxide (AAO) Templates on ITO Glass. *ACS Nano* **2008**, *2*, 2250−2256.
(35) Lee, W.; Park, S.-J. Porous Anodic Aluminum Oxide: Anodization and Templated Synthesis of Functional Nanostructures. *Chem. Rev.* **2014**, *114*, 7487−7556.
(36) Berryman, J. G. Random Close Packing of Hard Spheres and Disks. *Phys. Rev. A* **1983**, *27*, 1053−1061.
(37) Saliba, M.; Matsui, T.; Seo, J.-Y.; Domanski, K.; Correa-Baena, J.-P.; Nazeeruddin, M. K.; Zakeeruddin, S. M.; Tress, W.; Abate, A.; Hagfeldt, A.; Grätzel, M. Cesium-Containing Triple Cation Perovskite Solar Cells: Improved Stability, Reproducibility and High Efficiency. *Energy Environ. Sci.* **2016**, *9*, 1989−1997.
(38) Jia, J.; Dong, J.; Shi, B.; Wu, J.; Wu, Y.; Cao, B. Postpassivation of $Cs_{0.05}(FA_{0.83}MA_{0.17})_{0.95}Pb(I_{0.83}Br_{0.17})_3$ Perovskite Films with Tris-(pentafluorophenyl)borane. *ACS Appl. Mater. Interfaces* **2021**, *13*, 2472−2482.
(39) Caprioglio, P.; Wolff, C. M.; Sandberg, O. J.; Armin, A.; Rech, B.; Albrecht, S.; Neher, D.; Stolterfoht, M. On the Origin of the Ideality Factor in Perovskite Solar Cells. *Adv. Energy Mater.* **2020**, *10*, 2000502.
(40) Tress, W.; Yavari, M.; Domanski, K.; Yadav, P.; Niesen, B.; Baena, J. P. C.; Hagfeldt, A.; Graetzel, M. Interpretation and Evolution of Open-Circuit Voltage, Recombination, Ideality Factor and Subgap

https://doi.org/10.1021/acsaem.2c00870
ACS Appl. Energy Mater. 2022, 5, 11977−11986

Defect States During Reversible Light-Soaking and Irreversible Degradation of Perovskite Solar Cells. *Energy Environ. Sci.* **2018**, *11*, 151−165.
(41) Saliba, M.; Etgar, L. Current Density Mismatch in Perovskite Solar Cells. *ACS Energy Lett.* **2020**, *5*, 2886−2888.
(42) Sandberg, O. J.; Kurpiers, J.; Stolterfoht, M.; Neher, D.; Meredith, P.; Shoaee, S.; Armin, A. On the Question of the Need for a Built-In Potential in Perovskite Solar Cells. *Adv. Mater. Interfaces* **2020**, *7*, 2000041.
(43) Bergmann, V. W.; Guo, Y.; Tanaka, H.; Hermes, I. M.; Li, D.; Klasen, A.; Bretschneider, S. A.; Nakamura, E.; Berger, R.; Weber, S. A. L. Local Time-Dependent Charging in a Perovskite Solar Cell. *ACS Appl. Mater. Interfaces* **2016**, *8*, 19402−19409.
(44) Pitarch-Tena, D.; Ngo, T. T.; Vallés-Pelarda, M.; Pauporté, T.; Mora-Seró, I. Impedance Spectroscopy Measurements in Perovskite Solar Cells: Device Stability and Noise Reduction. *ACS Energy Lett.* **2018**, *3*, 1044−1048.
(45) Yoo, S.-M.; Yoon, S. J.; Anta, J. A.; Lee, H. J.; Boix, P. P.; Mora-Seró, I. An Equivalent Circuit for Perovskite Solar Cell Bridging Sensitized to Thin Film Architectures. *Joule* **2019**, *3*, 2535−2549.
(46) Futscher, M. H.; Lee, J. M.; McGovern, L.; Muscarella, L. A.; Wang, T.; Haider, M. I.; Fakharuddin, A.; Schmidt-Mende, L.; Ehrler, B. Quantification of Ion Migration in $CH_3NH_3PbI_3$ Perovskite Solar Cells by Transient Capacitance Measurements. *Mater. Horiz.* **2019**, *6*, 1497−1503.
(47) Reichert, S.; An, Q.; Woo, Y.-W.; Walsh, A.; Vaynzof, Y.; Deibel, C. Probing the ionic defect landscape in halide perovskite solar cells. *Nat. Commun.* **2020**, *11*, 6098.
(48) Horcas, I.; Fernández, R.; Gómez-Rodríguez, J. M.; Colchero, J.; Gómez-Herrero, J.; Baro, A. M. WSXM: A Software for Scanning Probe Microscopy and a Tool for Nanotechnology. *Rev. Sci. Instrum.* **2007**, *78*, 013705.
(49) Mínguez-Bacho, I.; Rodríguez-López, S.; Asenjo, A.; Vázquez, M.; Hernández-Vélez, M. Self-Correlation Function for Determination of Geometrical Parameters in Nanoporous Anodic Alumina Films. *Appl. Phys. A: Mater. Sci. Process.* **2012**, *106*, 105−112.

https://doi.org/10.1021/acsaem.2c00870
ACS Appl. Energy Mater. 2022, 5, 11977−11986